Nuclear Materials and Energy 18 (2019) 35–40

Contents lists available at ScienceDirect

Nuclear Materials and Energy

journal homepage: www.elsevier.com/locate/nme

Elemental and topographical imaging of microscopic variations in deposition on NSTX-U and DIII-D samples

C.H. Skinner[a,*], C.P. Chrobak[b], M.A. Jaworski[a], R. Kaita[a], B.E. Koel[c]

[a] Princeton Plasma Physics Laboratory, POB 451, Princeton, NJ 08543, USA
[b] General Atomics, PO Box 85608, San Diego, CA 92186-5608, USA
[c] Department of Chemical and Biological Engineering, Princeton University, Princeton, NJ 08540, USA

ARTICLE INFO

Keywords:
Erosion
Deposition
NSTX-U
DiMES
Plasma-materials interaction
Surface analysis

ABSTRACT

Tokamak plasma facing components have surface roughness that can cause microscopic spatial variations in erosion and deposition and hence influence material migration, erosion lifetime, dust and tritium accumulation, and plasma contamination. However, high spatial resolution measurements of deposition on a sub-μm scale of surface roughness have been lacking to date. We will present elemental images of graphite samples from NSTX-U and DIII-D DiMES experiments performed with a Scanning Auger Microprobe at sub-micron resolution that show strong microscopic variations in deposition and correlate this with 3D topographical maps of surface irregularities. The NSTX-U samples were boronized and exposed to deuterium plasmas. The DiMES samples had localized Al and W films and were exposed to dedicated helium plasmas. Topographical maps of the samples were performed with a 3D confocal optical microscope and compared to the elemental deposition pattern. The results revealed localized deposition concentrated in areas shadowed from the ion flux, incident in a direction calculated by taking account of the magnetic sheath.

1. Introduction

Tokamak plasma facing components (PFCs) have intrinsic surface roughness from their manufacturing process, and the roughness can increase with plasma exposure due to arc tracks and cracks from thermal stress. The surface roughness will influence erosion and deposition and hence material migration, erosion lifetime, dust and tritium accumulation, and plasma contamination. A key factor is the shallow angle of incidence of the magnetic field on the PFC surface which is often of order a few degrees so as to reduce the thermal power flux density. Ions traveling toward the surface accelerate, gyrate, and ExB-drift while falling into the sheath. For plasma facing surfaces with a magnetic field incident at angles less than about 5°, the Chodura or magnetic sheath controls the trajectory of the ions near the surface and leads to shallow angles of ion incidence. This has been modeled with fluid [1], kinetic [2], and PIC calculations [3]. A shallow angle of incidence for ions makes the detailed surface topology of rough PFC surfaces a critical factor in the resulting patterns of erosion and net deposition. Experimentally, deposition has studied by Rutherford Backscattering (RBS) and Scanning Electron Microscopy (SEM) on Asdex [4] and JET [5]. Model calculations of erosion and redeposition on rough surfaces were presented in reference [6] and found to be in good agreement with the Asdex data. Recently micro-ion beam analysis with a spatial resolution around 10 μm has been applied to JET tiles [7,8] and aluminum migration studied on DIII-D using the DiMES probe [9]. However elemental measurements of net deposition with a spatial resolution on the sub-micron scale of the surface roughness have been lacking.

In this paper we present elemental images of deposition on NSTX-U and DiMES graphite samples performed with Scanning Auger Microscopy (SAM) at sub-micron resolution that show strong microscopic variations. Topographical measurements of the sample surface were performed with a 3D confocal light microscope and compared to the elemental deposition pattern. The DiMES samples had localized Al and W films and were exposed to dedicated He plasmas. The NSTX-U samples had been boronized and exposed to deuterium plasmas. The role of oxygen impurities has been investigated via X-ray photoelectron spectroscopy (XPS) in a separate study of some NSTX-U samples [10].

2. Sample history

NSTX has recently undergone a major upgrade to NSTX-U [11] in order to explore low collisionality regimes and develop the physics basis for a ST-based Fusion Nuclear Science Facility. During the 2016

* Corresponding author.
E-mail address: cskinner@pppl.gov (C.H. Skinner).

https://doi.org/10.1016/j.nme.2018.12.001
Received 28 July 2018; Received in revised form 30 November 2018; Accepted 1 December 2018
2352-1791/ © 2018 The Authors. Published by Elsevier Ltd. This is an open access article under the CC BY-NC-ND license (http://creativecommons.org/licenses/BY-NC-ND/4.0/).

NSTX-U campaign a total of 117 g of dTMB (deuterated trimethylboron) [12] in a 5% dTMB/ 95% He mix, was injected into glow discharges for wall conditioning. A variety of L-mode and H-mode discharge were used in 16 weeks of NSTX-U initial plasmas [13]. Altogether, there were 1138 discharges with plasma current above 50 kA and the total integrated plasma duration was 845 s.

On the DIII-D tokamak the DiMES manipulator [14] was used to expose an ATJ graphite substrate to a series of repeated lower single null, ohmic low density attached helium L-mode, Te ~15 eV plasmas near the outer strike point [9]. Specific regions on the sample had been coated with Al or W in order to measure erosion and material migration. The aluminum was used as a proxy for beryllium, the tungsten coating was used to measure erosion by carbon impurity ions. RBS, bandpass-filtered Al I and SEM imaging were applied to characterize the net erosion and compare it to modeling. The results suggested an accumulation or trapping of redeposited Al in surface pores and other areas shadowed from re-erosion [15].

3. Scanning Auger microscopy and 3D optical microscopy

A Scanning Auger Electron Microprobe (SAM) [16] combines a Scanning Electron Microscope (SEM) with an electron energy analyzer that selects electrons at a specific kinetic energy to probe Auger electrons from the distribution of electron energies emitted from the sample and uses these characteristic electrons for elemental imaging. While the SEM electron beam penetrates about a micron into the sample, Auger electrons that are emitted with kinetic energies in the 50–1500 eV range have an inelastic mean free path (imfp) in graphite of 0.30–1.5 nm [17]. This limits the observed Auger electron signals to come from a sampling depth, generally taken to be three times the imfp or 1–5 nm, that is particularly well-suited to studying deposited layers with thicknesses in the nm range. The advantage of SAM over other surface analysis techniques such as RBS or XPS, is the much higher spatial resolution that results from using a highly focused electron beam that can be scanned over the surface to create elemental images with SEM-like resolution. A limitation is that the flux of Auger electrons is low compared to the total secondary electron flux available for SEM imaging, and long scan times (up to 2.5 d) were needed for high pixel mapping (e.g. 512 × 512).

The instrument used in the present study was a Thermo Scientific™ Microlab 310-F, that had been upgraded with Avantage control and data acquisition software. It has a double focussing spherical sector electron energy analyzer and an EX05 scanning ion beam source for sputter cleaning and depth profiling. The electron beam energy was 10 keV and it was operated with the gun and objective apertures withdrawn to maximize the electron flux for fast elemental imaging with a sample current of typically 100 nA. The base vacuum pressure was in the range 4–9 × 10^{-9} torr. The electron beam column is vertical and the electron analyzer and ion gun are at 30° and 34° respectively above horizontal. The sample stage is typically horizontal but can be tilted in a range 20° forward and 90° backward (toward the analyzer).

The 310-F analyzer has five channeltron detectors and can operate either in a spectral mode with the electron beam stationary on the sample and the analyzer energy scanned for Auger electron spectroscopy (AES), or an imaging mode with the electron beam scanned over the sample and the analyzer energy fixed. Characteristic Auger electron peaks were identified by means of standard databases within the instrument's Avantage software. The software performs elemental quantification by integrating under a spectral line after background subtraction using the Shirley method [18] with an additional constraint that the background should not be of a greater intensity than the actual data at any point in the region. A sensitivity factor modified by the instrument transmission function is used to calculate the atomic percent concentration. For SAM imaging, acquiring spectral line information at every pixel would take a prohibitive length of time. Instead the analyzer energy and the retard ratio (electron kinetic energy / analyzer pass energy) is fixed at a value so the five channeltron energies span both the Auger electron peak and the neighboring background. The electron beam was then scanned over the sample with a dwell time of 1 s for each pixel, and a total scan time for a full 512 × 424 pixel image of 60.3 h.

Two optical confocal microscopes were used for topographical measurements of the sample surface. An Olympus LEXT OLS4000 microscope was used for 3D measurements of the DiMES sample surfaces. The LEXT instrument is a confocal measuring microscope with a 405 nm diode laser and six objective lenses from x5 to x100. A Leica DCM3D confocal microscope with objective lenses from x5 to x150 was used for the NSTX-U C15 sample. The manufacturer specifies a lateral resolution of 0.14 μm for the x150 objective used for Fig. 9.

4. Aluminum migration on the DiMES sample

Polished graphite samples with areas coated with 80 nm thick aluminum and 16 nm thick tungsten films were exposed to a sequence of DIII-D L-mode plasmas using the DiMES facility. Full experimental details are given in references [9,15]. The graphite samples had a surface roughness of ~600 nm with deep pores 5–50 μm in diameter covering ~10% of the surface. Fig. 1(a) shows an optical image of one-half of the 46 mm diameter DiMES probe 'RHe' with a W coated

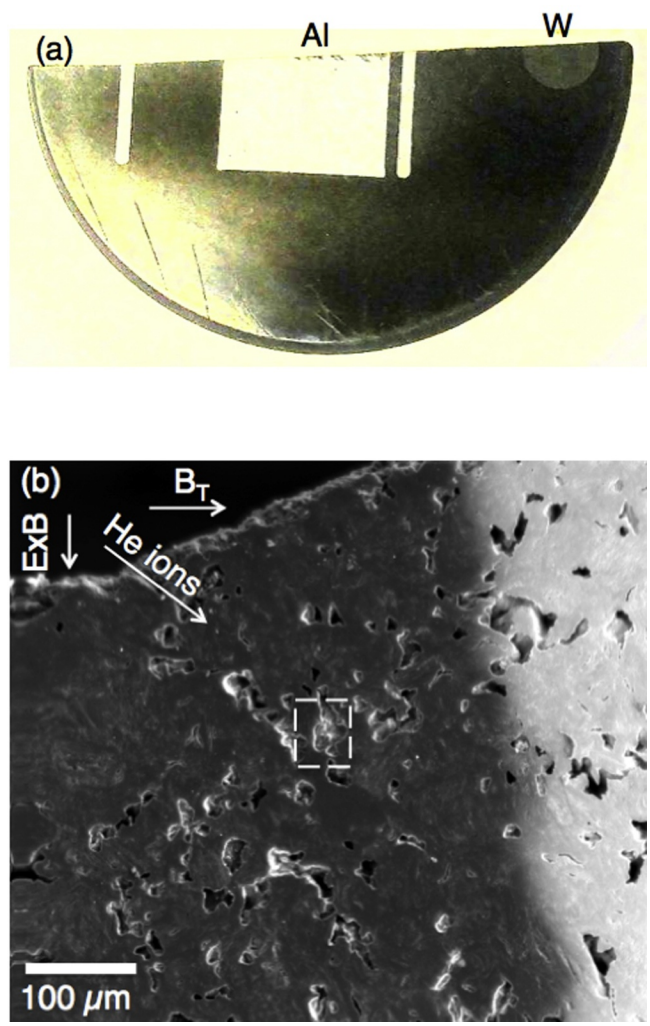

Fig. 1. (a) Optical image of the 46 mm diameter section of the polished graphite DiMES sample "RHe" with the Al stripes and W semicircular coating indicated, and (b) a SEM image of the area next to the W coating with the B_T, ExB and azimuthal incident He ion directions in DIII-D [15] shown. The dashed rectangle denotes the area imaged in Fig. 3.

semicircle at the upper right. Two core samples were obtained using a custom-made 9.5 mm diameter coring drill. These samples were drilled from the back side and then caught in a special tray to ensure no debris from the drilling operation contaminated the surface. The plasma facing top 2 mm of the cores was then removed in a special jig and the core samples stored without any material contacting the central region of the core surface. Fig. 1(b) shows a SEM image of the graphite surface with the edge of the W-coated area on the right and the pore imaged in the present paper in a dashed rectangle. The W boundary and sample cut line enable a clear identification of the sample orientation and the toroidal field and ExB direction in DIII-D as indicated on the figure.

The incident ion angle distribution on the sample in DIII-D was calculated in reference [15] using a Monte-Carlo particle tracking method, accounting for sheath potential gradients in a magnetized sheath with a 1–2° angle between the magnetic field and surface plane. The azimuthal angle of incidence is indicated in Fig. 1(b). The majority of ions are predicted to strike the horizontal DiMES surface at $<15°$ with respect to the surface plane, in a direction 30–60° radially inboard from the toroidal field (when projected on the horizontal plane), after drifting 1–3 cm in the $E \times B$ direction. This leads to highly asymmetric sputtering angular distributions and ion flux shadowing on upstream areas of rough surfaces.

The sample was introduced into the Microlab 310-F with a horizontal stage orientation and initial AES spectra were taken of 6 points on the surface and pores of the area shown in Fig. 1(b). AES survey scans identified C, O, Al, and W signals. The 310-F magnification was then increased to image the pore shown in the dashed box. This pore is 8 mm from the nearest Al stripe and 0.17 mm from the adjacent W spot. AES spectra were taken of an additional 89 points in this area. Ion beam sputtering was not used in these measurements to avoid any possibility of uneven etching of the rough surface. Quantitative analysis using AES showed an inhomogeneous Al concentration (3%–29%) inside the pore and a low Al concentration (4%–6%) on the surface outside the pores. The energy limits and background used for AES analysis are shown in grey in Fig. 2. Unsurprisingly, the highest W concentration (44%) was found on the W-coated spot. Tungsten measured on the polished graphite surface had a much lower concentration (2%–15%), however it ranged up to 30% inside the pores. The balance of the sample surface was composed of oxygen (including presumably oxides of W and Al) and carbon. A 30-point AES line scan using a 0.3 μm step size over the central "mound" circled in Fig. 3(a) showed the Al concentration varied smoothly by a factor of four from 3–13% over a distance of 3 μm.

A (512 × 424) pixel SAM image of Al was then obtained by

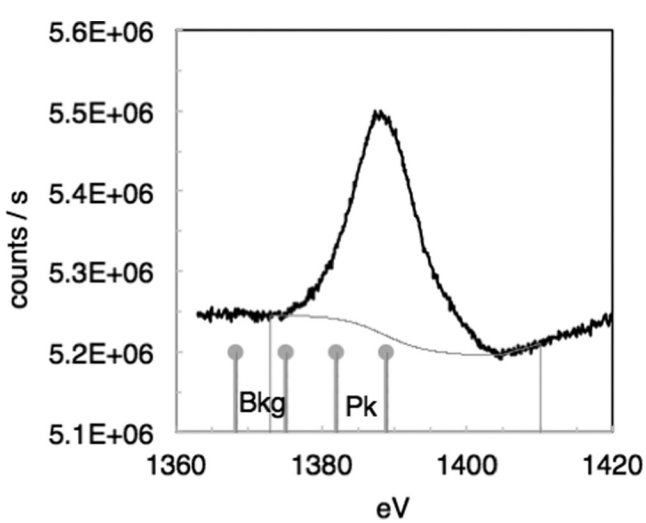

Fig. 2. Aluminum KLL Auger lineshape with energies of two background and two peak channeltrons marked. The energy limits and background used for AES analysis are shown as a grey line.

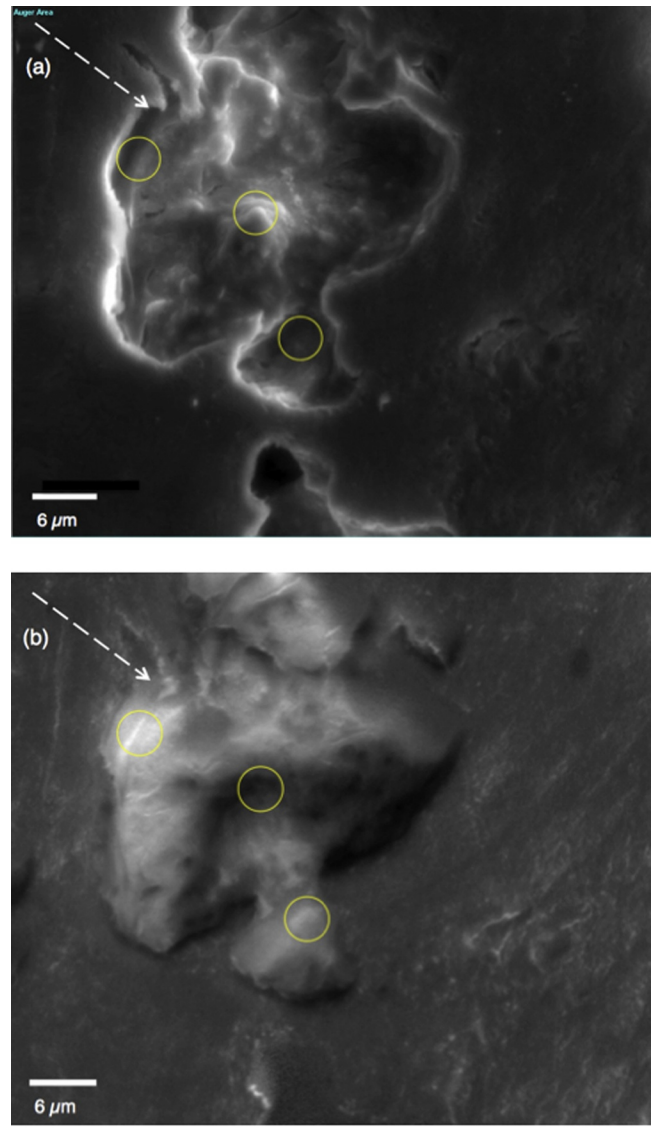

Fig. 3. (a) SEM image of pore inside the white dashed rectangle in Fig. 1(b) and (b) corresponding SAM image of aluminum deposition. The circles are intended to aid comparison of the images. The azimuthal incident He ion direction in DIII-D is indicated by the dashed arrow.

rastering the electron beam with the center analyzer energy fixed and a retard ratio of 5, using channeltron energies of 1368.2 eV and 1375.1 eV (background), and 1382.0 eV and 1388.9 eV (Al KLL peak) as shown in Fig. 2. Fig. 3 compares (a) the SEM image and (b) an aluminum image generated from the (peak − background) / (peak + background) signals; (for more information on the algorithms used to form a SAM image see reference [16]). The grey scale in Fig. 3(b) was expanded so the image intensity approximately spans the atomic densities measured in the AES line scans. The azimuthal incident He ion direction in DIII-D as calculated in reference [15] is shown by an arrow in Fig. 3. Similar Al SAM images of the wide area shown in Fig. 1(b) were also generated together with a high magnification image of different pores. These all showed a similar deposition pattern that was concentrated on upstream surfaces that were shadowed from the incident He ions.

An Olympus OLS4000 confocal microscope was used to characterize the 3D geometry of selected pores. The sample was mounted with the surface as close as possible to horizontal and the stage moved so that the field of view corresponded to the pore shown in Fig. 3. White light and 3D confocal images were recorded. Fig. 4 shows a 3D image of the

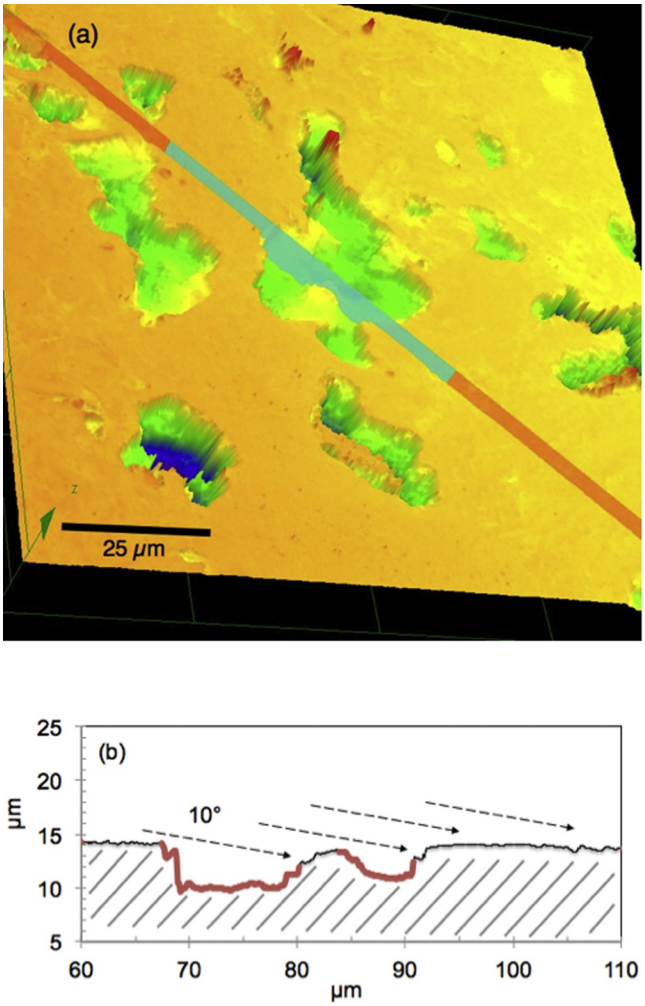

Fig. 4. (a) Topographic image of area surrounding pore shown in Fig. 3 and (b) depth profile following the indicated line in the DIII-D B-field direction across the pore. The scale bar in (a) corresponds to 25 μm. The dashed arrows in (b) represent an incidence angle of 10° and the thicker lines (colored red on-line) represent the corresponding shadowed areas of the surface. (For interpretation of the references to color in this figure legend, the reader is referred to the web version of this article.)

pore and surrounding surface recorded with the x100 objective and a depth profile generated across the sample in the incident ion direction. The profile reveals that the 'mound' visible at the center of both the SEM and optical images is 0.7 μm below the surface of the surrounding polished graphite. The thicker lines in Fig. 4(b) denote the upstream surfaces in the pore that are shadowed from particles incident at an incident angle of 10° The neighboring pore on right hand edge of the Fig 4(a) image was similar, i.e. 13 μm wide and 17 μm deep with a projection from the upstream edge of the pore to the downstream bottom of the pore to be 53° below horizontal.

The angle of incidence of the local magnetic field in DIII-D for this sample (R-He) is 1.4° [9] and the corresponding incident ion angle distribution was calculated to be 0–20° in reference [15] by taking account of the magnetic sheath. Comparing the incident ion angle to the pore geometry reported above, it is clear that downstream side of the pore wall is exposed to incident ions. The observed deposition pattern of aluminum is consistent with deposition and then re-erosion from the downstream sides of the pores with some of the eroded aluminum redeposited either deeper in the pores or on the upstream sides where it accumulates as it is shadowed from the incident ions and further erosion.

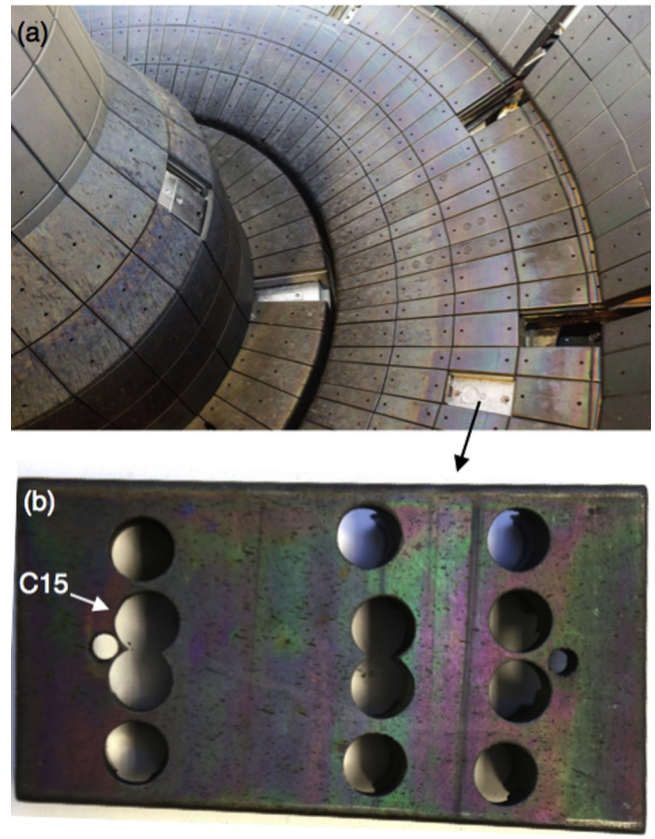

Fig. 5. (a) NSTX-U lower divertor after tiles were removed (the coloration is due to thin film interference), (b) The outboard lower divertor tile after coring; core C15, used in the present analysis, is indicated by an arrow.

5. Net boron deposition on NSTX-U samples

After the 2016 campaign, three graphite tiles were retrieved from representative regions in the NSTX-U vessel as shown in Fig. 5(a) plus one from the upper divertor, and 6–15 core samples were removed from each tile. The NSTX-U C15 sample from the outboard lower divertor tile area indicated in Fig. 5(b) was transferred to the SAM. An AES survey spectrum, Fig. 6(a), showed boron, carbon and oxygen peaks. The kinetic energy of the boron peak (173 eV) and the corresponding sampling depth (1 nm) are comparatively low. A light Ar ion etch (0.2 μA/mm^2 for 10 s) with the stage tilted 30° toward the ion beam revealed an increased B concentration (from 5% to 7.5%). Further etching did not noticeably increase the B concentration at this location. A high resolution elemental scan of the boron line is shown in Fig. 6(b). The comparatively small B peak and sloping background creates some uncertainty in the absolute B concentration, however the strong variation in the B concentration is very clear in the AES line scans. Fig. 7 shows the B, C and O concentrations derived from a north-south line scan over the area circled in the B SAM image in Fig. 5 (here 'north' refers to the directional convention used in geographical maps). The derived B atomic concentration in this scan varied over a factor of five, from 2% to 10%. At other locations the B concentration ranged up to 16%.

The SAM electron energy analyzer was set to have a retard ratio (electron kinetic energy / analyzer pass energy) of unity to enable the five channeltrons to span the B KLL Auger peak and the background. The channeltron energies used were 171.0, 175.5, 180.0, 184.5, and 189.0 eV as indicated in Fig. 6(b). A boron SAM image was created from the ratio (P-B)/(P + B) where the average of signals from the first four channels is denoted 'P' for Peak and signal from the 5th channel 'B' for Background. The grey scale in the image was adjusted to span the variation in B concentration observed in the AES line scans. A SEM

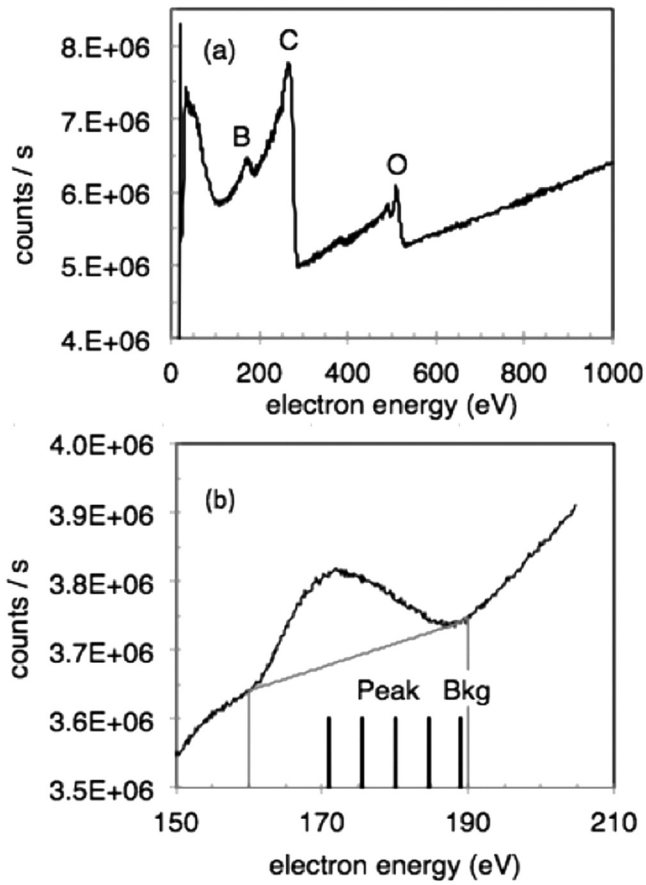

Fig. 6. (a) AES survey spectrum from NSTX tile sample C15 with boron, carbon and oxygen Auger peaks marked; (b) Boron KLL Auger lineshape with the analyzer energies marked for the four Peak channeltrons and one Background channeltron used for Fig. 8. The energy limits and background used for AES analysis are shown as a grey line.

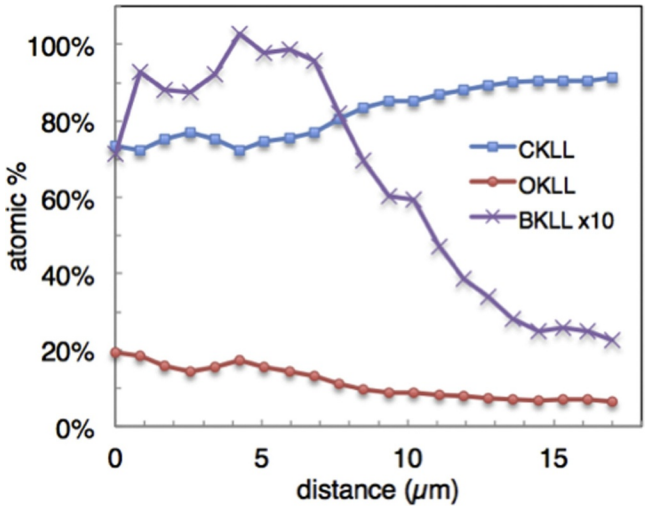

Fig. 7. Surface concentration in atomic % of carbon, oxygen and boron (scaled x10) derived from AES along a north-south line scan across the circled area in Fig. 8.

image and a boron SAM image of the same area is shown in Fig. 8. Comparison of the two images reveals a strong boron concentration on northward facing slopes.

NSTX-U tiles were exposed to a variety of plasma conditions during the FY16 campaign [13]. An approximate estimate of the campaign

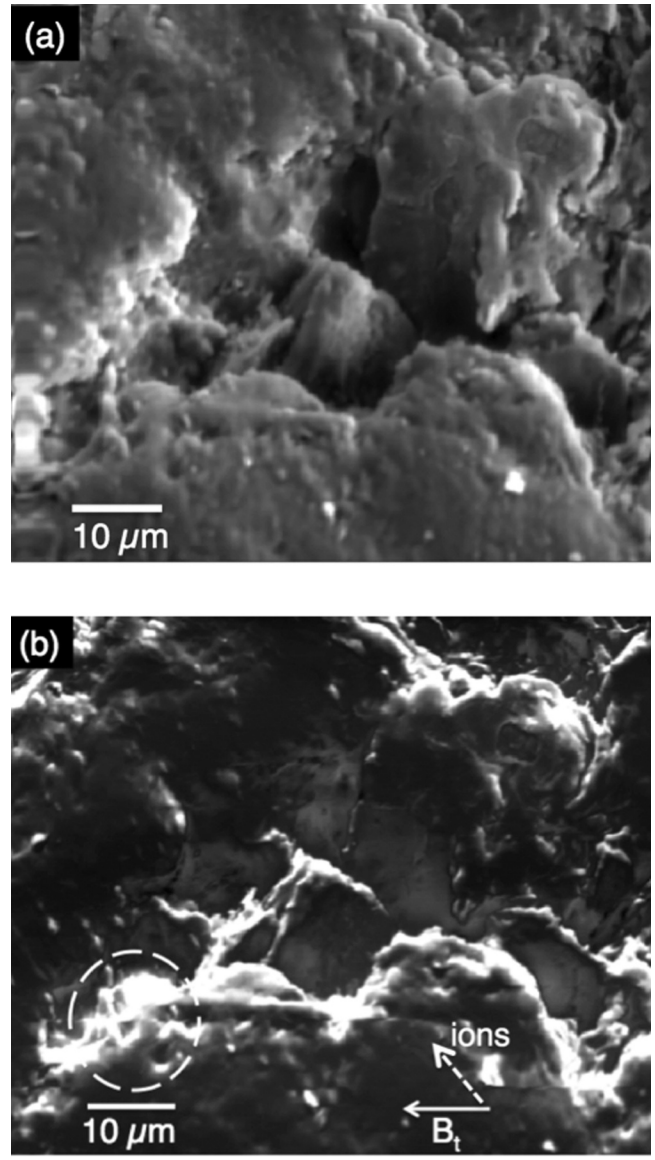

Fig. 8. (a) SEM image of pore in NSTX-U C15 sample; (b) SAM image of same area using the boron KLL Auger emission intensity. A north-south linescan across the circled area is shown in Fig. 7. The approximate direction of the toroidal B field and azimuthal incident ion direction are indicated.

averaged angle of incidence of the magnetic field at the location of the C15 sample (major radius, R = 0.687 m) was made using EFIT [19] for discharges where the strike point was within 6 cm of the sample. The angle was calculated every ~6 ms and the data set was filtered to remove points with plasma currents less than 100 kA and with anomalous ohmic heating power as reported by magnetic reconstructions. Twenty one boronizations [12] were applied weekly or daily throughout the campaign and this was taken to be a constant factor. The resulting 23,718 data points yielded an average angle of incidence of the magnetic field of 10.5° (std. dev. = 2.2°) with respect to the sample surface. The incident ion angle was calculated using the methodology of [15] for a magnetic field incident angle of 10.5° (with respect to the surface plane), for cases with electron temperature, Te 10, 20, or 30 eV and electron density, Ne = 1, 2, or 3E19 m^3 (local measurements are not available). In contrast to the DIII-D DiMES case above, the magnetic field angle in all these cases is greater than the critical angle at which the Debye sheath would be negligible, so there is still a partial Debye sheath near the surface. Because of this, the average polar incident angle is about 45° (with respect to surface normal). The distribution of

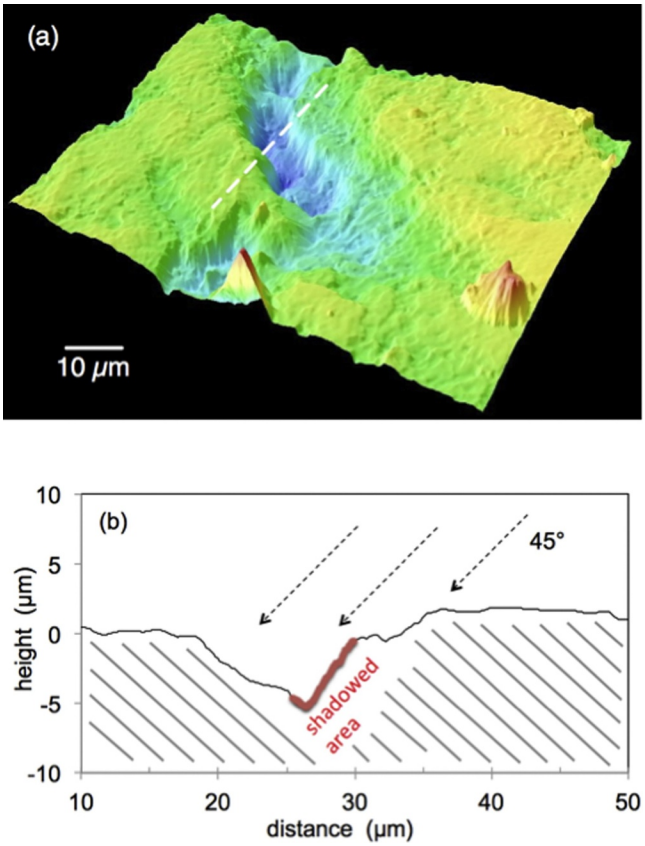

Fig. 9. (a) Topographical 3D images of arc track on NSTX-U sample C15 in the vicinity of the area shown in Fig 8. (b) Height profile along the white dashed line in (a). The dashed arrows in (b) represent an incidence angle of 45° and the thicker line (colored red on-line) represent the corresponding shadowed areas of the surface. (For interpretation of the references to color in this figure legend, the reader is referred to the web version of this article.)

polar incident angles has a width of about 15°. The azimuthal incident angle distribution is broader, ranging from about −25° to −75°, peaking around −50° (with respect to toroidal direction).

The north-west ward facing slopes of the pores (using the map convention above) that are steeper than ~ 45° in the C15 sample surface in Fig. 8 would then be shadowed from the incident ions from the plasma leading to a buildup of deposits of re-eroded boron. In contrast, the southward facing slopes would be exposed to incident ions and any boron deposits could be re-eroded. The pattern of net deposition observed in Fig. 8(b) is consistent with erosion and deposition by ions incident in the direction shown.

The NSTX-U C15 sample was transferred to a Leica DCM3D confocal microscope for 3D imaging of the surface. A sub-mm piece of Cu tape was attached to edge of the sample surface to help identify the sample orientation, however the small SEM field (< ½ mm), and the different SEM and optical contrast mechanisms, together with the paucity of uniquely identifiable surface features made it very difficult to navigate the optical microscope to the exact same area imaged by the SEM. Dead reckoning was used instead and Fig. 9 shows a topographical image of an arc track in the vicinity of Fig. 8. Fig. 9(b) shows the height profile along the dashed line in Fig. 9(a). In Fig. 9(b) dashed lines are shown corresponding to incoming particles at 45° incidence angle, and the area in the arc track that is shadowed from such particles is shown by a thicker line. Measurements of other features showed pore depths of up to 20 μm with similar shadowed areas.

6. Conclusions

Erosion and deposition has wide ranging consequences for tokamaks through material migration, PFC erosion lifetime, dust and tritium accumulation, and plasma contamination. Strong microscopic variations in deposition were measured in elemental imaging of NSTX-U and DIII-D DiMES graphite samples surfaces at sub-micron resolution using scanning Auger microscopy (SAM). These variations were correlated with surface irregularities that were measured in 3D by optical confocal microscopy. For both NSTX-U and DIII-D DiMES samples net deposition was concentrated in areas shadowed from the plasma ions that were incident in a direction calculated by taking account of the magnetic sheath. Surface roughness is an important factor in modeling material migration however a predictive understanding is challenging as both the sheath conditions and the detailed surface topology are complex and are not practically possible to diagnose in situ.

Acknowledgments

The authors thank William Wampler for bringing this topic to the authors (CS) attention. They acknowledge important contributions from Doug Labrie and Gus Smalley in operating the Thermo Microlab SAM and from Ron Bell in image data analysis. The Leica DCM3D confocal microscope was available through the PRISM Imaging and Analysis Center. We thank Prof. Craig Arnold's group and especially Emre Turkoz for assistance with the Olympus LEXT confocal microscope. Support was provided by the U.S. DOE, Contract nos. DE AC02-09CH11466, DE-AC52-07NA27344 and DE-NA0003525. The digital data for this paper can be found in http://arks.princeton.edu/ark:/88435/dsp011v53k0334

Supplementary materials

Supplementary material associated with this article can be found, in the online version, at doi:10.1016/j.nme.2018.12.001.

References

[1] P.C. Stangeby, Nucl. Fusion 52 (2012) 083012.
[2] D. Coulette, G. Manfredi, Plasma Phys. Control. Fusion 58 (2016) 025008, , https://doi.org/10.1088/0741-3335/58/2/025008.
[3] R. Khaziev, D. Curreli, Phys. Plasmas 22 (2015) 043503.
[4] M. Mayer, V. Rohde, G. Ramos, E. Vainonen-Ahlgren, J. Likonen, J.L. ChenASDEX Upgrade team, Phys. Scr. T128 (2007) 106, https://doi.org/10.1088/0031-8949/2007/T128/021.
[5] M. Mayer, et al., J. Nucl. Mater. 363–365 (2007) 101.
[6] K. Schmid, et al., Nucl. Fusion 50 (2010) 105004.
[7] M. Tokitani, et al., Fusion Eng. Des. 116 (2017) 1–4.
[8] Y Zhou, et al., Nucl. Mater. Energy 12 (2017) 412.
[9] C.P. Chrobak, et al., Nucl. Mater. Energy 12 (2017) 441.
[10] F. Bedoya, Ph.D. Thesis, University of Illinois at Urbana-Champaign, 2017.
[11] J.E. Menard, et al., Nucl. Fusion 57 (2017) 102006https://doi.org/10.1088/1741-4326/aa600a.
[12] C.H. Skinner, et al., Nucl. Mater. Energy 12 (2017) 744 http://dx.doi.org/10.1016/j.nme.2016.11.024.
[13] D.J. Battaglia, et al., Nucl. Fusion 58 (2018) 046010https://doi.org/10.1088/1741-4326/aaa6e0.
[14] C.P.C. Wong, et al., J. Nucl. Mater. 196–198 (1992) 871–875.
[15] C.P. Chrobak, et al., Nucl. Fusion 58 (2018) 106019https://doi.org/10.1088/1741-4326/aad4c9.
[16] Scanning Auger Electron Microscopy, in: M. Prutton, M.M. El Gomati (Eds.), Scanning Auger Electron Microscopy, John Wiley and Sons Ltd, Chichester UK, 2006.
[17] C.J. Powell, A. Jablonski, NIST Electron Inelastic-Mean-Free-Path Database – Version 1.2, National Institute of Standards and Technology, Gaithersburg, MD, 2010https://www.nist.gov/srd/nist-standard-reference-database-71.
[18] D.A. Shirley, Phys. Rev. B. 5 (1972) 4709.
[19] S.A. Sabbagh, S.M. Kaye, J.E. Menard, et al., Nucl. Fusion 41 (2001) 1601.